Integrated Sentinel-1 InSAR and GNSS Time-Series Along the San Andreas Fault System

Xiaohua Xu, David T. Sandwell, Emilie Klein, Yehuda Bock

JGR Solid Earth

RESEARCH ARTICLE
10.1029/2021JB022579

Integrated Sentinel-1 InSAR and GNSS Time-Series Along the San Andreas Fault System

Xiaohua Xu[1], David T. Sandwell[2], Emilie Klein[3], and Yehuda Bock[1]

[1]Institute for Geophysics, University of Texas at Austin, Austin, TX, USA, [2]Institute of Geophysics and Planetary Physics, Scripps Institution of Oceanography, University of California San Diego, La Jolla, CA, USA, [3]Laboratoire de géologie - CNRS UMR 8538, Ecole normale supérieure - PSL Université, Paris, France

Key Points:

- A practical approach is developed to integrate Sentinel-1 Interferometric Synthetic Aperture Radar and Global Navigation Satellite System time-series over the entire San Andreas fault system
- The product is used to estimate fault creep and three components of horizontal crustal strain which shows notable off-fault portion
- Challenges remain in separating tectonic and hydrologic sources and whether hydrologic strain will increase seismic hazards

Supporting Information:

Supporting Information may be found in the online version of this article.

Correspondence to:

X. Xu,
xiaohua.xu@austin.utexas.edu

Citation:

Xu, X., Sandwell, D. T., Klein, E., & Bock, Y. (2021). Integrated Sentinel-1 InSAR and GNSS time-series along the San Andreas fault system. *Journal of Geophysical Research: Solid Earth*, *126*, e2021JB022579. https://doi.org/10.1029/2021JB022579

Received 10 JUN 2021
Accepted 27 OCT 2021

Author Contributions:

Conceptualization: Xiaohua Xu, David T. Sandwell
Data curation: Xiaohua Xu
Formal analysis: Xiaohua Xu
Funding acquisition: David T. Sandwell, Yehuda Bock
Investigation: Xiaohua Xu
Methodology: Xiaohua Xu, David T. Sandwell
Project Administration: David T. Sandwell, Yehuda Bock
Resources: Xiaohua Xu, David T. Sandwell, Emilie Klein, Yehuda Bock
Software: Xiaohua Xu
Supervision: David T. Sandwell, Yehuda Bock
Validation: Xiaohua Xu, Emilie Klein
Visualization: Xiaohua Xu

Abstract Measuring crustal strain and seismic moment accumulation, is crucial for understanding the growth and distribution of seismic hazards along major fault systems. Here, we develop a methodology to integrate 4.5 years (2015–2019.5) of Sentinel-1 Interferometric Synthetic Aperture Radar (InSAR) and continuous Global Navigation Satellite System (GNSS) time series to achieve 6 to 12-day sampling of surface displacements at ~500 m spatial resolution over the entire San Andreas fault system. Numerous interesting deformation signals are identified with this product (video link: https://www.youtube.com/watch?v=SxNLQKmHWpY). We decompose the line-of-sight InSAR displacements into three dimensions by combining the deformation azimuth from a GNSS-derived interseismic fault model. We then construct strain rate maps using a smoothing interpolator with constraints from elasticity. The resulting deformation field reveals a wide array of crustal deformation processes including, on- and off-fault secular and transient tectonic deformation, creep rates on all the major faults, and vertical signals associated with hydrological processes. The strain rate maps show significant off-fault components that were not captured by GNSS-only models. These results are important in assessing the seismic hazard in the region.

Plain Language Summary Seismic hazard models rely on accurate measurements of small motion over large areas on the Earth's crust. Traditional geodetic models based on Global Navigation Satellite System (GNSS) data cannot resolve small scale deformation patterns, mainly due to expensive and limited station deployment. Interferometric Synthetic Aperture Radar (InSAR) has become the emerging tool for mapping surface deformation, with its advantages of low-cost and full-coverage. Yet InSAR measurements, compared to GNSS, come with larger biases from the atmospheric noise, especially over length scales greater than 80 km. Here, we combined the two methods to resolve fine spatial scales and achieve high accuracy. Our results are presented as deformation time-series over the entire San Andreas fault system (video link: https://www.youtube.com/watch?v=SxNLQKmHWpY). From these deformation time series, we have estimated fault creep rates and strain accumulation. One important finding is that there is significant off-fault strain, though we suspect this is mainly due to hydrological processes. These results will advance our knowledge of the earthquake cycle, strain/moment accumulation, and the associated seismic hazards.

1. Introduction

An improved understanding of how energy and seismic moment accumulate in the crust and upper mantle along major plate boundaries is essential for forecasting the size and timing of major earthquakes (Field et al., 2015; Rollins et al., 2020; Smith-Konter & Sandwell, 2009; Weiss et al., 2020). Recent studies have shown that most damaging earthquakes occur in areas where the crustal strain rate exceeds 100 nanostrain/yr (e.g., Bayona et al., 2021; Elliott et al., 2016; Zeng et al., 2018). Many of these areas are heavily populated and have been struck by major destructive earthquakes in the past (Ward et al., 2021). Moreover, one of the largest uncertainties in earthquake hazard models (e.g., California's UCERF-3 model (Field et al., 2014, 2015) is the amount of plate boundary deformation that is accommodated by off-fault strain and whether this strain is accumulating as elastic or plastic deformation. Therefore, accurate strain rate measurements are needed to improve earthquake forecasts. Achieving an ideal 100-nanostrain/yr accuracy in California at an ideal 10-km resolution (i.e., the typical fault locking depth) requires a horizontal velocity model that has an accuracy of 1 mm/yr. Besides, moderate earthquakes, fault creep, and other

Writing – original draft: Xiaohua Xu
Writing – review & editing: Xiaohua Xu, David T. Sandwell, Emilie Klein, Yehuda Bock

transient processes produce temporal variations in strain rate that commonly exceed 100-nanostrain/yr (Holt and Shcherbenko, 2013; Klein et al., 2019). Currently continuous Global Navigation Satellite System (GNSS) network in California can provide vector deformation better than the required 1 mm/yr accuracy but do not have uniform 10 km spacing between stations. Interferometric Synthetic Aperture Radar (InSAR) provides very high spatial resolution but cannot achieve the 1 mm/yr accuracy, mainly due to atmospheric noise (Emardson et al., 2003). In addition, current InSAR systems provide only two components of surface deformation and thus cannot uniquely distinguish between horizontal and vertical strain (Shen and Liu, 2020). Here, we develop a path to achieving the time-dependent strain rate mapping objective by combining 4.5 years of measurements from InSAR and GNSS along the San Andreas fault system (SAFS) (Figure S1 in Supporting Information S1).

The accuracy and spatial resolution of the current strain rate models derived from GNSS velocities can be assessed by comparing results from various groups. An accuracy analysis was performed as part of the developing SCEC Community Geodetic Model (CGM-V1; Sandwell, Zeng et al., 2016). Seventeen models were taken from previous publications (Field et al., 2014; Flesch et al., 2000; Hackl et al., 2009; Kreemer et al., 2014; Loveless & Meade, 2011; McCaffrey, 2005; Parsons, 2006; Parsons et al., 2013; Petersen et al., 2008, 2014; Platt & Becker, 2010; Sandwell & Wessel, 2016; Shen et al., 2015; Smith-Konter & Sandwell, 2009; Tape et al., 2009; Tong et al., 2014; Zeng & Shen, 2016). The mean and standard deviation of the 10 well-correlated models are shown in Figure 1a. Those that were not selected have either incomplete coverage or significant deviations from the rest of the models. Note that the standard deviation (Figure 1b) commonly exceeds 50 nanostrain/yr especially above the major faults where the uncertainties can exceed 100 nanostrain/yr. These significant deviations among the models are not due to inaccuracies in the GNSS data but to the incomplete spatial coverage of the GNSS stations, which is typically 10–20 km in California (Wei et al., 2010).

To further characterize this lack of sufficient spatial resolution of the strain rate field, we analyzed the then strain rate models by computing cross spectra in their overlapping region in Southern California. Radially averaged cross spectra were computed between every pair of models using Generic Mapping Tools (GMT; Wessel et al., 2019). As illustrated in Figure 1c, there is a large variation in the coherence between these models. Most models agree well at long wavelengths, but generally disagree at short wavelengths, except those having very similar, or identical, fault models like Shen et al. (2015) and Zeng and Shen (2016) or Tong et al. (2014) and Smith-Konter and Sandwell (2009). The disagreements are due to different physical modeling approaches, assumed fault geometries, and slightly different GNSS velocity data sets. For most pairs, the coherence is high at very long wavelength and decreases to zero coherence at ~10 km. The 0.2 coherence threshold (Bendat & Piersol, 2011) of the median of all the cross spectra is located at 30–40 km wavelengths.

2. Methods

Our InSAR/GNSS integration approach is an extension of standard published methods (e.g., Tong et al., 2013; Weiss et al., 2020) although in addition to long-term secular velocity, we also calculate line-of-sight (LOS) displacement time series (e.g., Neely et al., 2019). The GNSS weekly displacements were derived by means of a median filter (Klein et al., 2019) of daily time series estimated as part of a NASA MEaSUREs project (Bock et al., 2021). Moreover, we use the secular velocity from a GNSS-only interseismic model (Zeng & Shen, 2017) to create semi-vertical vector InSAR time series from the LOS displacements. A brief description of the method follows:

1. Gather Sentinel-1 Terrain Observations with Progressive Scans (TOPS) data from multiple tracks and re-assemble into common re-defined frames, typically 250 km by 500 km.
2. Geometrically co-register all SAR acquisitions and construct all interferograms with perpendicular baseline <150 m and temporal separation <90 days (Sandwell, Xu et al., 2016; Xu et al., 2017).
3. Mask bodies of water and areas of persistent low coherence regions and replace them with nearest-neighbors (Shanker & Zebker, 2009). This step improves the phase unwrapping accuracy which is done with Statistical-Cost, Network-Flow Algorithm for Phase Unwrapping (Chen & Zebker, 2002).
4. Perform elevation dependent atmospheric phase correction (Elliott et al., 2008). Compute the difference between the remaining InSAR phase and projected 3-component GNSS weekly solutions (Klein

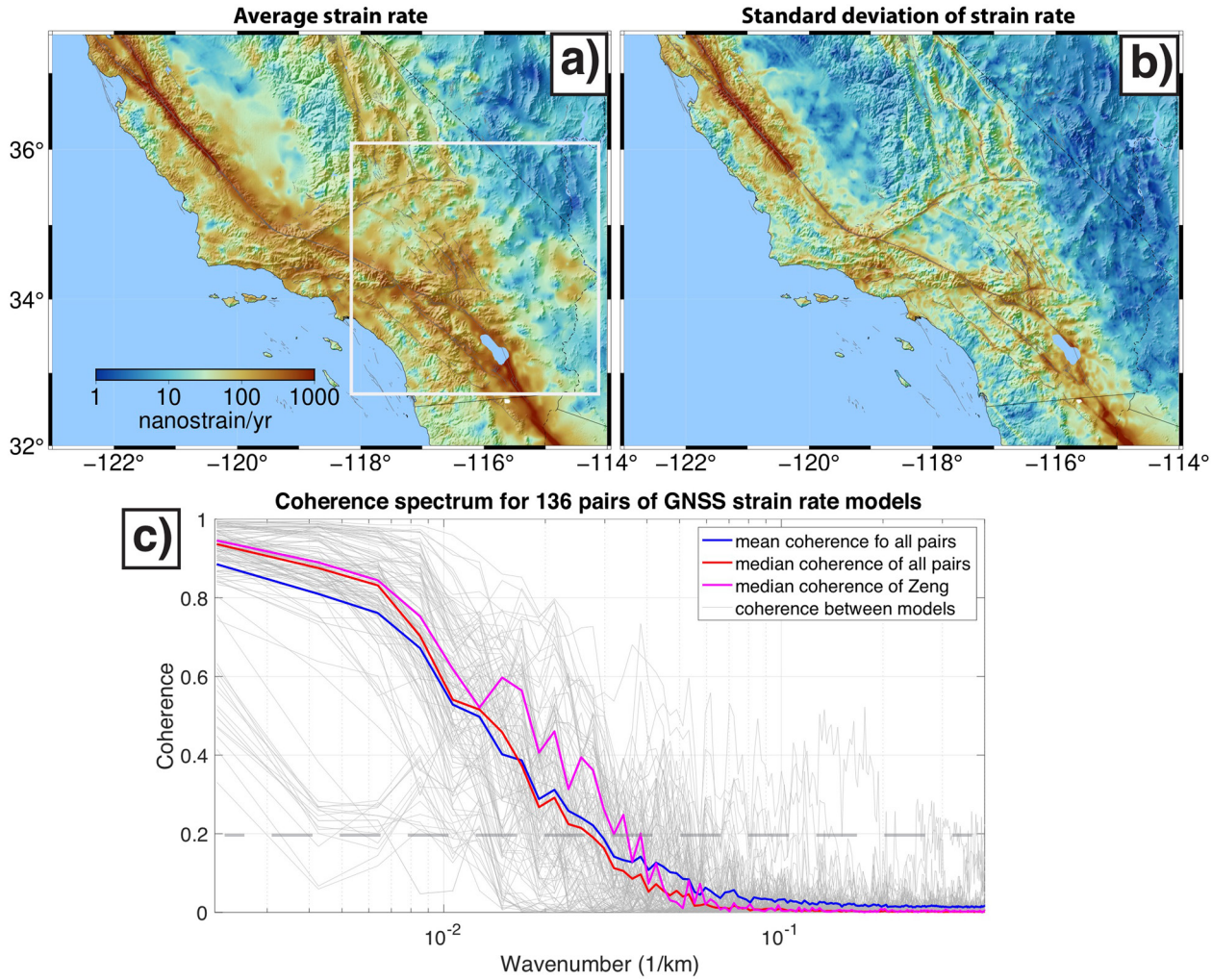

Figure 1. Second invariant of the horizontal strain rates from Global Navigation Satellite System models (Sandwell, Zeng et al., 2016). (a) Average of 10 "best" models based on a spatial correlation analysis. (b) Standard deviation of the 10 models. (c) Radially averaged cross spectra between all pairs of SCEC CGM-V1 strain rate models, performed in the area denoted by the white box in panel (a). The mean and median of all the spectra have a 0.2 coherence at wavelengths of 30–40 km. Our objective for accurate strain-rate measurement is to maintain at least 0.2 coherence among the models, at a 10 km spacing, when integrated with Interferometric Synthetic Aperture Radar.

et al., 2019), interpolate this difference, filter at 80-km wavelength and remove this difference from each interferogram. After this step, the unwrapped interferograms are tied to GNSS.

5. Construct time-series using a coherence-based SBAS approach integrated with atmospheric phase correction using common-scene stacking (Tong & Schimdt, 2016; Tymofyeyeva & Fialko, 2015; Xu et al., 2017).
6. Subtract a horizontal GNSS velocity model (e.g., Zeng & Shen, 2017) from the time-series to create semi-vertical InSAR time-series.

Since Sentinel-1 TOPS data is acquired under burst acquisition mode and there is occasional inconsistency in data coverage, especially in the early days of the mission, the frame boundaries in step 1 are chosen considering both spatial coverage and acquisition numbers. The total number of interferograms generated in step 2 is 5,230, connecting acquisitions from 910 dates over 9 tracks. Enhanced spectral diversity (Prats-Iraola et al., 2012) is not performed in step 2, since it will remove an expected tectonic signal that will eventually supply a third deformation component (Li et al., 2021), as compared to what InSAR phase measures, it is mostly sensitive to motion along North-South. The estimated mis-registration could be up to 2/1,000 pixel/yr along SAFS and spread across the scenes, where a constant shift from ESD is inadequate,

while the performance of bivariate approach (Wang et al., 2017) is yet to be evaluated. Moreover, the common scene stacking time series approach (step 5) is capable of mitigating along-track orbital errors by absorbing burst discontinuities, that are random in time, into atmospheric phase screens (Xu et al., 2017). The nearest-neighbor interpolation in step 3 is implemented so phases are allowed to vary properly along very long coastlines, and stay connected through the snowy Sierras and heavy vegetation in northern California. The elevation dependent component in step 4 is assumed as a bivariate quadratic polynomial function thus spatial variations in atmospheric contribution are accounted for (Elliott et al., 2008). The relatively large, 80-km wavelength filter, that is applied to the GNSS correction for each interferogram, is sufficient to absorb the large-scale atmospheric and orbital errors affecting the InSAR displacements and also to accommodate areas such as the Central Valley that have sparse GNSS coverage. The later data masking was done by examining phase closures with respect to each pixel, with any pixels having over 30% non-closure triplets removed (Xu & Sandwell, 2019). A remove-restore approach (Tong et al., 2013) using a purely horizontal secular velocity model is not used because it is incompatible with the significant vertical signal in Central Valley. Not only is this vertical deformation distributed over hundreds of kilometers, but it also has a sharp transition around the edges of the sedimentary basins. The interpolation of discrepancies between GNSS and InSAR is adopted here, taking advantage of the notion that although the vertical deformation changes dramatically over a large area, the differences from the two type of observations are likely systematic and vary slowly enough in space to be well evaluated. When the final velocity is computed, the first and last four records are not used, mainly because the atmospheric correction approach gains less constraints when acquisitions are non-evenly distributed (Tymofyeyeva & Fialko, 2015).

3. Analysis, Results, and Discussion

3.1. Average Velocity

The integrated Sentinel-1 InSAR and GNSS time-series reveals a complex time-averaged velocity field over the entire SAFS (Figures 2 and 3). The most prominent feature is the large-scale tectonic motion across the diffuse plate boundary with sharp transitions at creeping strike-slip faults and broader transitions at more deeply locked faults. The descending track data exhibit a clear transition crossing the faults while the ascending track transition is less evident. This is partially due to the acquisition geometry where the fault motion has a smaller portion mapped into the satellite LOS, but also because the acquisition times for the ascending tracks in California are usually at sun-set when the atmosphere is more turbulent (descending acquisitions are usually in the morning). Superimposed on this tectonic pattern are numerous nontectonic deformations mostly related to hydrological and hydrothermal processes. These non-tectonic features are highlighted in the semi-vertical component (Figure 2d). Our velocity maps are available as kmz files so that the user can examine in detail the correlations between vertical deformation and natural and man-made surface features (file link: http://topex.ucsd.edu/gmtsar/tar/San_Andreas_Xu_et_al.kmz; see Text S1 in Supporting Information S1 and Movie S1 for much more details).

3.2. LOS Time Series

We have compared the integrated InSAR/GNSS LOS time series with the GNSS-only time series and find both excellent and poor agreement (Table S2 in Supporting Information S1). Note the two time-series will not match exactly as our approach is essentially trusting the GNSS data at long wavelengths (>80km) and the InSAR data at short wavelengths (<80km). Figure 4b shows several examples where there is excellent agreement between the InSAR and GNSS time-series. The typical deviation of GNSS daily solutions from its moving average is around 3–4 mm, while the integrated InSAR deviation is only slightly larger, around 3–6 mm (Figure 4a). The vertical component could largely reproduce this deviation and can be considered as the major source of discrepancy. However, there are a number of cases where the integrated InSAR GNSS time-series fail to match the GNSS solutions (Figure 4c). In most cases, this is a direct result of anomalous displacements or artifacts in the GNSS displacement time series. An extreme example is station P800 in Los Angeles, which shows systematic effects due to the growth of thick vegetation nearly concealing the GNSS antenna and causing a significant drift in the north direction over a period of about 2 years (overlapping with the 4.5 years of our time series) until the vegetation is cleared in May 2018. Station CRHS is also in Los Angeles and is affected by vegetation, and the data after 2006 are suspect and should not be used - the

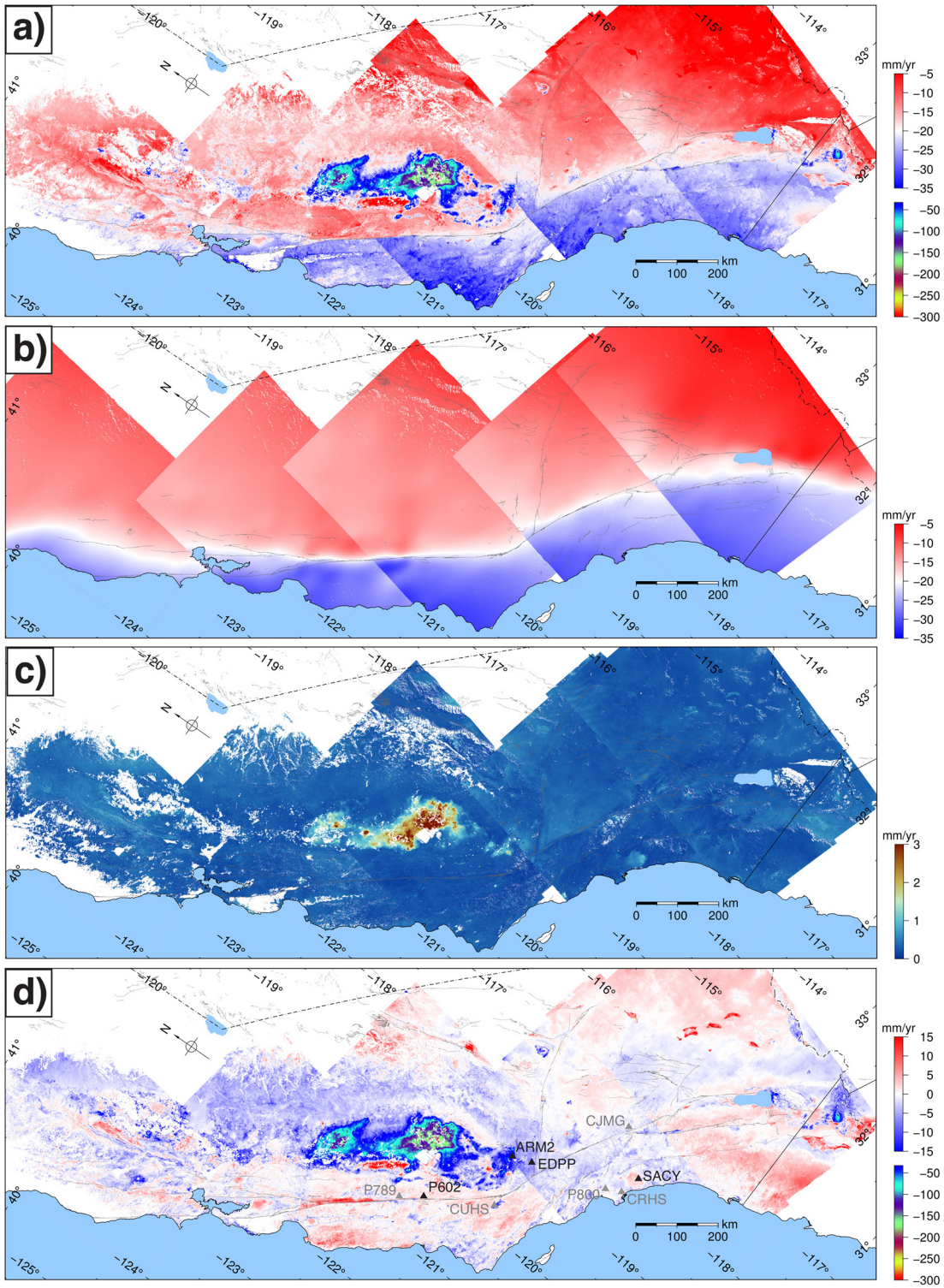

Figure 2. Line-of-sight (LOS) deformation velocity (descending) along the San Andreas fault system. (a) Total LOS deformation velocity with red color denoting motion toward the satellite and blue away from the satellite. A second color scale is added to highlight the major subsidence in the Central Valley. (b) Horizontal Global Navigation Satellite System (GNSS) velocity derived using gpsgridder (Sandwell & Wessel, 2016) projected into the LOS (for illustration purposes only). (c) Velocity variation/uncertainty is the deviation of the time series at each pixel from a linear regression fit. The velocity discontinuities between swaths are due to the change in look angle. (d) Semi-vertical velocity is the LOS with horizontal velocity model (Zeng & Shen, 2017) removed. The triangles in panel (d) mark the location of GNSS stations plotted in Figure 4b (black) and Figure 4c (gray).

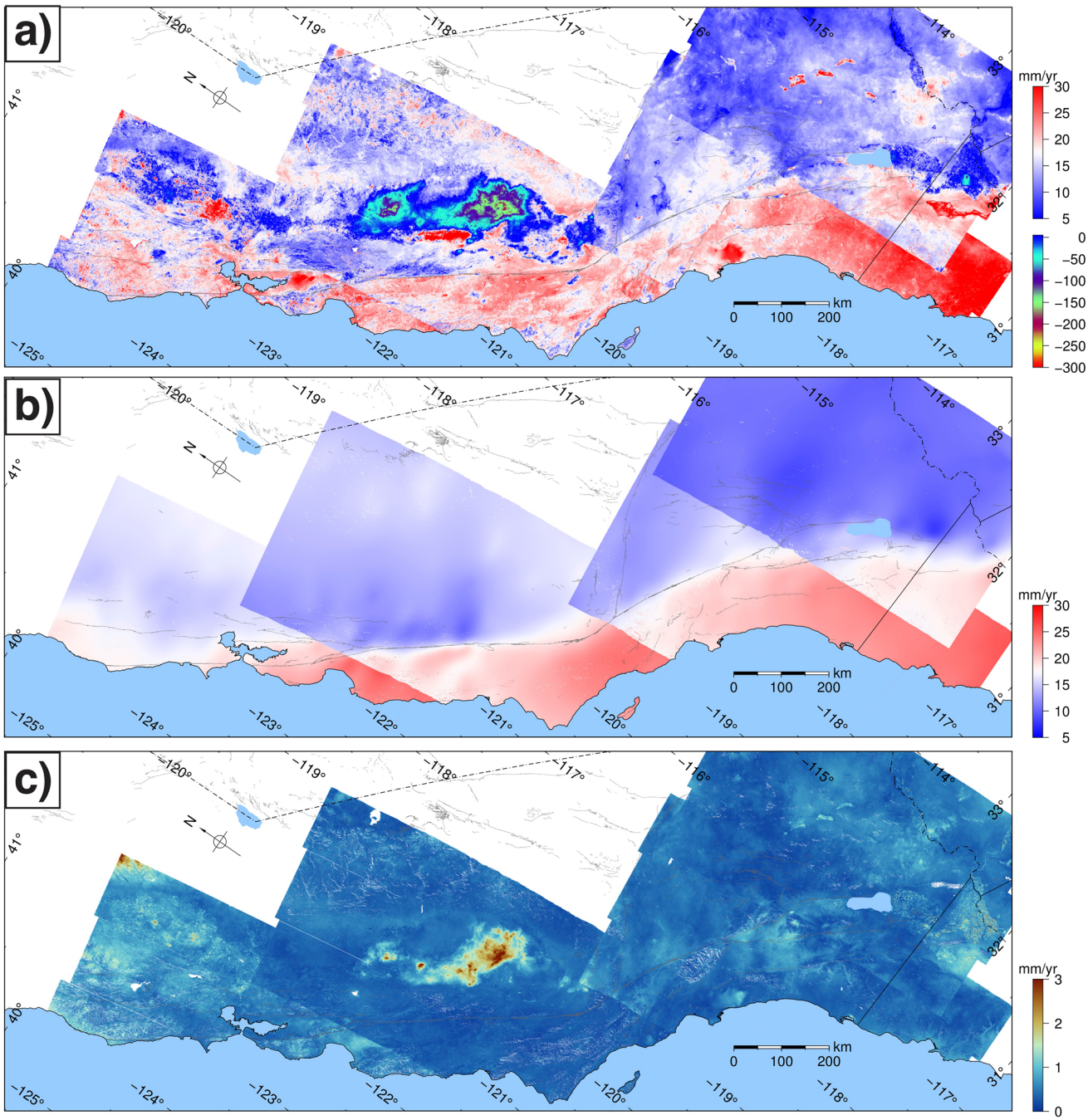

Figure 3. Line-of-sight deformation velocity (ascending) along the San Andreas fault system. Panels are the same as Figure 2, but for ascending the tracks.

station was subsequently abandoned. Station CUHS in the Cuyama Valley is subject to significant subsidence of about 30 mm/yr with a seasonal signature resulting in non-tectonic horizontal displacements with amplitudes up to 30 mm. Station CJMG in the San Gabriel Mountains has annual horizontal artifacts starting in 2017 with an amplitude of 30 mm (peak to peak). Another example is station P789 on the San Andreas fault in the transition zone between locked and creeping sections, which is experiencing uplift since 2013 of about 2.5 mm/yr but is not fully sufficient to explain its misfit with InSAR. For the purpose of this study, these GNSS anomalous data were not excluded. Rather, we allowed for discrepancies to persist through the integration, especially when a single station shows large mismatch, because the GNSS correction model, applied to each interferogram, is smoothed with a robust filter that down weighs the anomalous

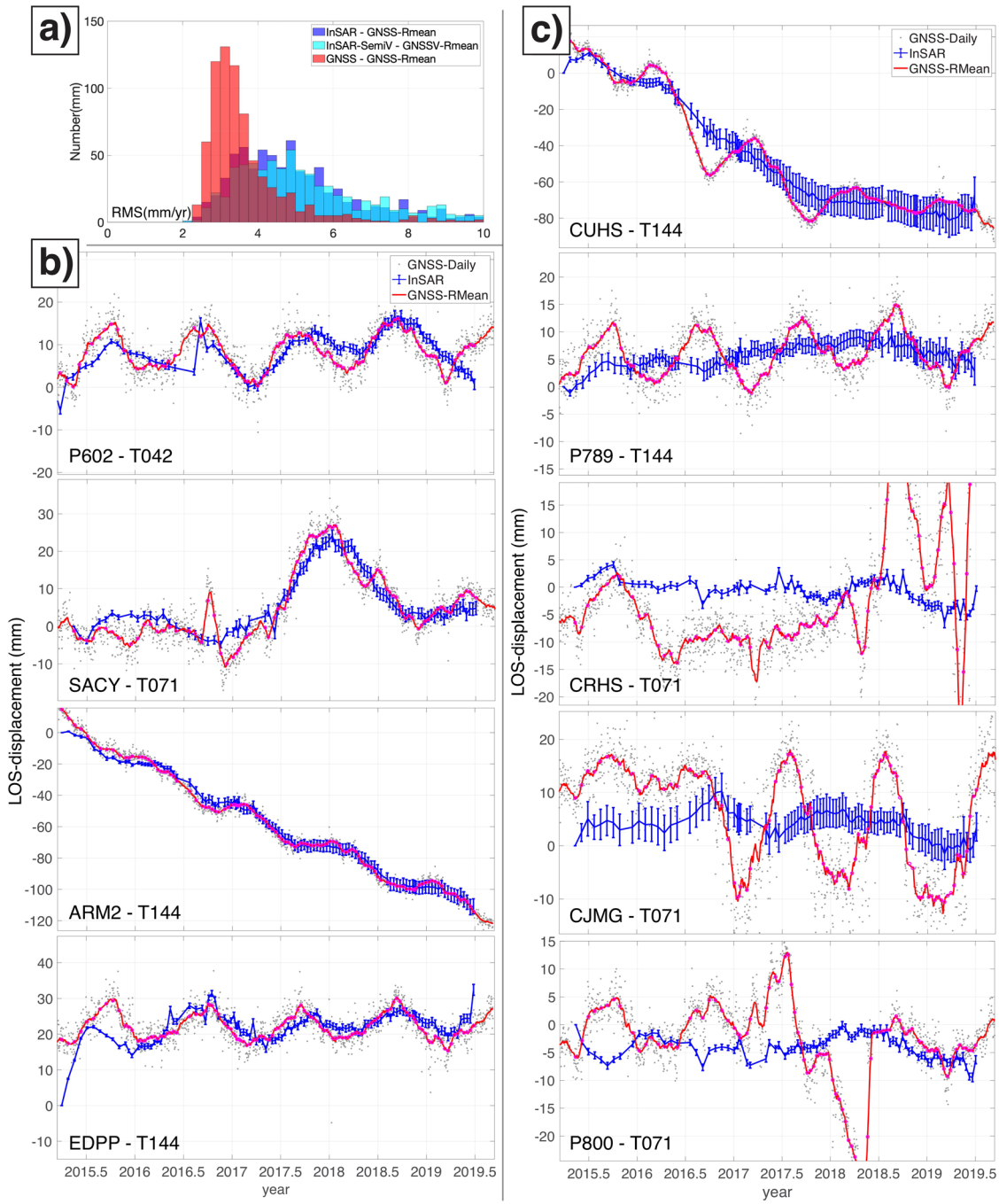

Figure 4. Comparisons of Interferometric Synthetic Aperture Radar (InSAR) line-of-sight (LOS) time series with Global Navigation Satellite System (GNSS) time series projected into the LOS. (a) Histograms of deviation from GNSS moving average (window 4 weeks). Red colors are for GNSS daily solution, blue for integrated InSAR and GNSS time-series, and cyan for the semi-vertical component in the integrated InSAR and GNSS time-series (horizontal GNSS model removed, comparison made with GNSS vertical component only). (b) Subplots of InSAR and GNSS time series at 4 GNSS stations showing good agreement after integration. Gray dots are GNSS daily solutions, blue curves are InSAR solutions after integration, and red curves are running mean GNSS with magenta circles denoting the samples associated with InSAR acquisition time. Uncertainties of InSAR time-series are standard deviations taken in 500-m boxes. (c) Subplots of InSAR and GNSS time series at 5 GNSS stations showing poor agreement after integration.

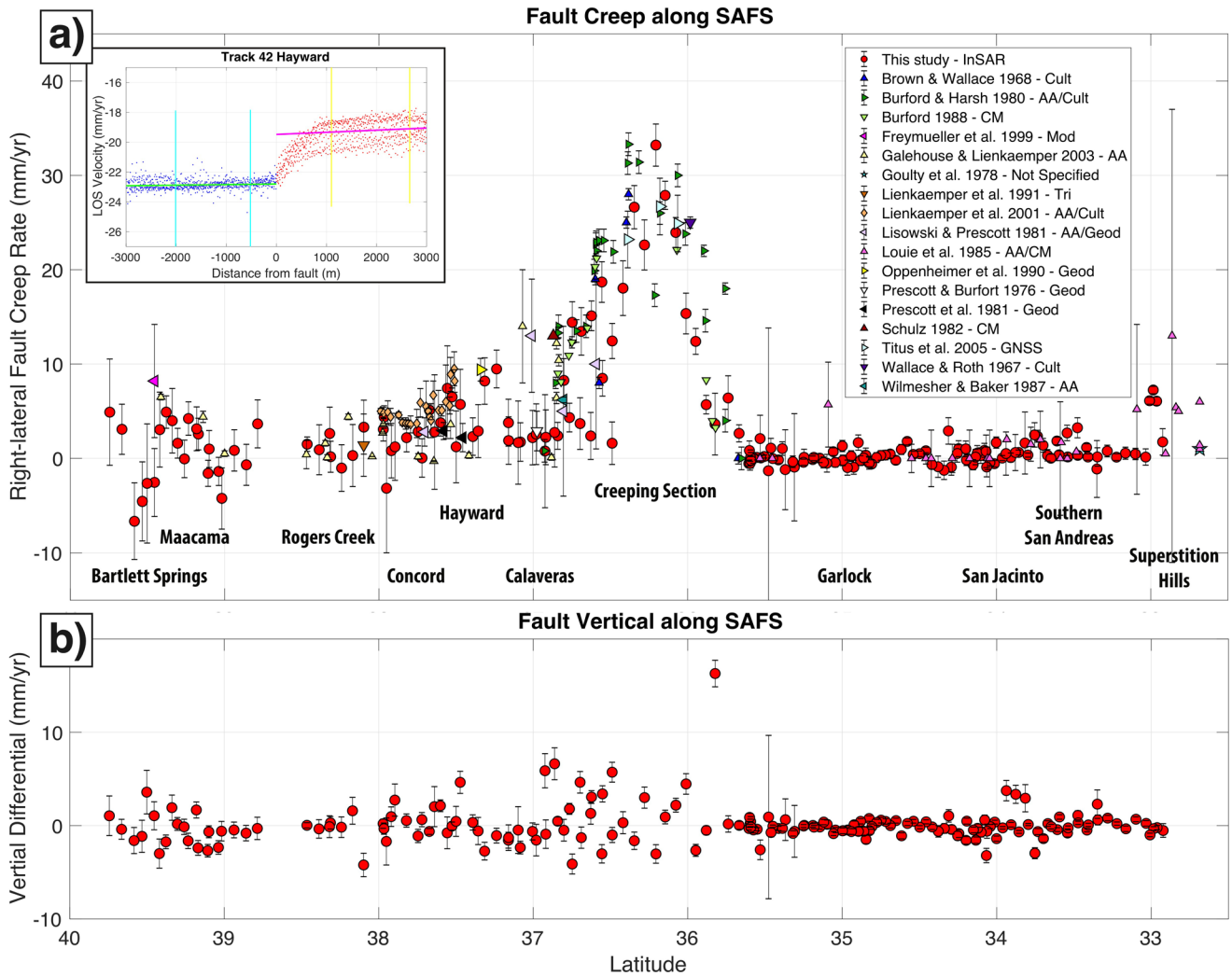

Figure 5. Comparison of creep rate estimates along major segments of the San Andreas fault system. (a) Red circles are right-lateral creep rates from decomposing two-look Interferometric Synthetic Aperture Radar (InSAR) line-of-sight estimates into fault parallel horizontal and vertical. Detailed estimates for each segment are available in Table S1 in Supporting Information S1. A compilation of creep estimates from Field et al. (2009) are also plotted with markers for each individual study listed in the upper right box. Survey types are listed as: AA-alignment array, CM-creep meter, Cult-cultural offset features, Geod-small geodetic array, Mod-inferred from model, and Tri-trilateration. The upper left box shows an example from a descending InSAR track covering Hayward fault, showing how the estimates are performed, with blue and red dots denoting data on the western and eastern side of the fault, and cyan and yellow bars denoting the selected region for estimation, and green and magenta lines are the fitted deformation profile used to estimate the offset. (b) Fault vertical differential in the creep rate estimates. Positive is defined as eastern side uplift (northern side up for Garlock fault).

misfits. Thus, if data from a GNSS station starts to behave anomalously, the InSAR time-series remain largely unaffected (Figure 4c). In further studies, we recommend a more conservative approach in choosing stations for the GNSS/InSAR integration. More assessment and results are available in Table S2 and Figure S2 in Supporting Information S1.

3.3. Fault Creep Rate

Fault creep rate can be estimated from just two components of LOS deformation if one assumes there is no fault-normal displacement (Xu et al., 2018). By making this assumption we measure the fault-parallel and vertical creep rate along each individual strand within the SAFS (Figure 5; Table S1 in Supporting Information S1). The method, which is similar to the Burford and Harsh (1980) method, is to fit a linear model to the LOS data over a flat area on each side of the fault (up to 3 km) and record the offset of the linear models at the fault location. The along-fault offset locations have a typical spacing of 10 km and roughly follow

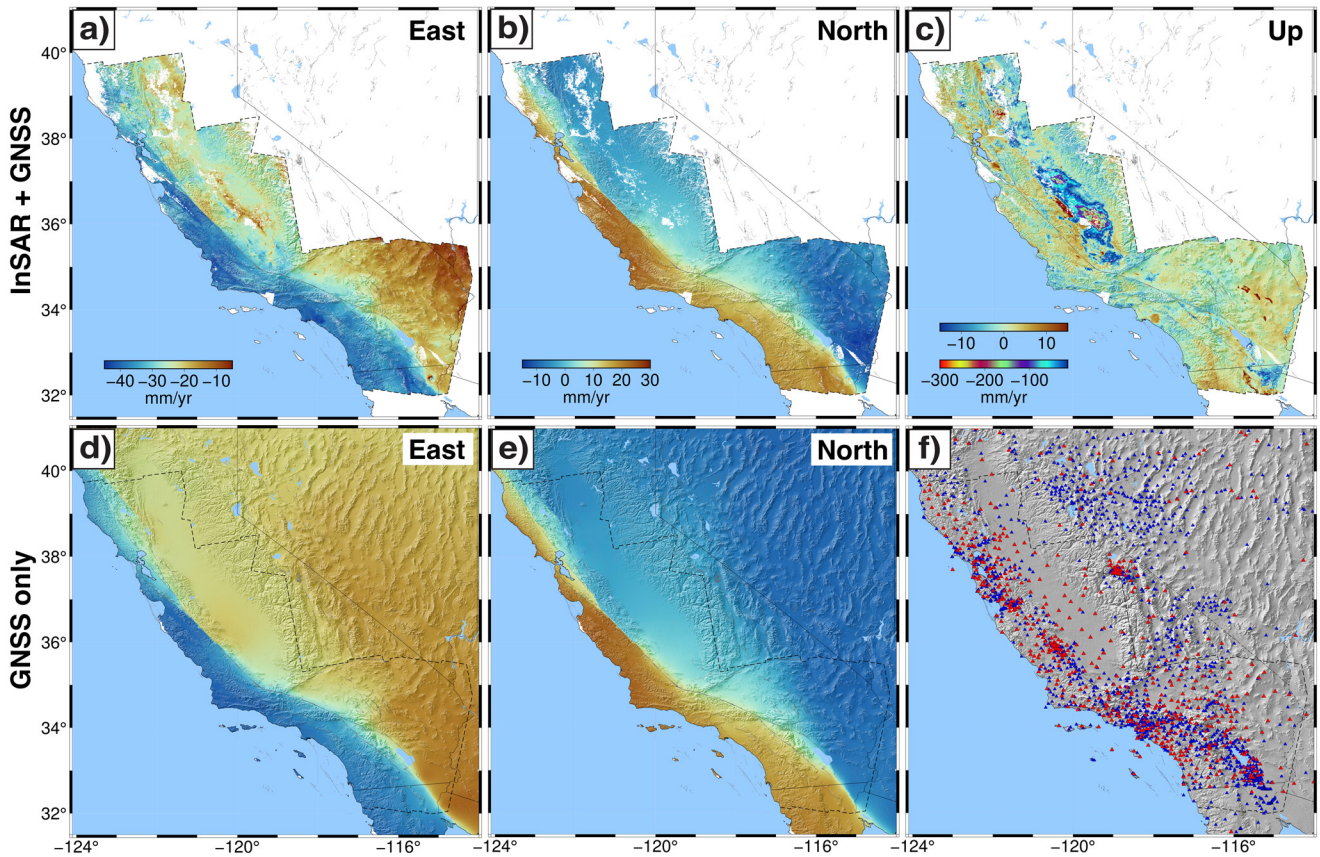

Figure 6. Surface vector velocity maps for the SAFS in the ITRF2014 coordinate system. Panels (a–c) are the decomposed east, north and vertical component respectively. Panels (d and e) are Global Navigation Satellite System (GNSS) horizontal velocity model from Zeng and Shen (2017), with same color-scales in Panels (a and b). Panel (f) is stations distributions, with blue triangle denoting GNSS campaign sites used in the GNSS model and red triangles denoting continuous sites used both in GNSS model and Interferometric Synthetic Aperture Radar (InSAR)/GNSS integration. Decomposition of InSAR GNSS integrated velocity maps uses horizontal deformation direction information provided by the model shown in panels (d and e).

the locations from the study of Tong et al. (2013). Some areas of fault creep have a velocity step up to 1 km wide; In these cases, the linear fit is confined to the flatter part of the LOS data on each side of the fault (e.g., Figure 5a, at Hayward fault). The fault creep rates estimated in this study are presented together with a compilation by Field et al. (2009) (Figure 5a). Fault vertical differential (Figure 5b) shows no systematic pattern along these faults. However, not accounting for the vertical offset will bias the horizontal offset estimates. A few larger vertical offsets (Figure 5b) are associated with subsidence at fault step-overs.

3.4. Velocity Decomposition

In order to compute the horizontal components of strain rate we must first construct three components of surface velocity (east, north, and up) from only two components of LOS velocity. To accomplish this, we adopt the assumption that the direction of surface displacement matches the direction from the GNSS velocity model (Shen & Liu, 2020; Tymofyeyeva & Fialko, 2018; Wright et al., 2004). This utilizes the local azimuth of a horizontal GNSS velocity field predicted from the interseismic slip model of Zeng and Shen (2017) as a constraint to reduce the required degrees of freedom in the measurements from three to two, thus a 3-D decomposition could be performed (Figure 6). Note that due to the near-polar orbits, InSAR satellites are generally not very sensitive to north-south motion. Thus, the decomposed north-south component absorbs most of its information from the GNSS model, resulting in an oversmoothed field (Figure 6b). The decomposed velocity field (Figure 6) reveals detailed spatial variations in the east-west component together with dramatic vertical motions. Some of the variations in the horizontal component are associated with hydrological signals (e.g., inside Central Valley). Subsidence inside the Central Valley is greater than

30 cm/yr with other areas like Geysers, Heber and Cerro Prieto Geothermal Fields standing out in the map. Uplifts at ground water recharging sites (Long Beach, Santa Clara Valley, etc.) is usually a direct reflection of human activities, some of which cannot be well represented by a single velocity (e.g., Figure 2c, GNSS station SACY). Note since the velocity is derived as a linear fit, a positive rate does not necessarily result from an overall uplift.

3.5. Strain Rate

The 3-D velocity maps derived from the InSAR/GNSS combination have small spatial scale variations that are associated with hydrological processes and residual atmospheric error. These models must be smoothed to extract the underlying tectonic strain rate (e.g., Pagani et al., 2021; Weiss et al., 2020). This is accomplished by using a smoothing interpolator that has constraints from elasticity to couple the two horizontal velocity components (Haines & Holt, 1993) as implemented in the GMT program *gpsgridder* (Sandwell & Wessel, 2016). We first subsample both the GNSS and InSAR/GNSS horizontal velocity fields shown in Figure 6 at a spacing of 2.5 km resulting in 40,016 2-D velocity estimates. The *gpsgridder* algorithm uses singular value decomposition of the elasticity Greens functions and we select only those associated with the largest 800 eigenvalues. We then compute the three horizontal strain rate components from the smoothed horizontal velocities, using the definition from Savage et al. (2001). A comparison of the GNSS only and InSAR/GNSS results for several components of strain rate (second invariant, maximum shear and dilatation) is shown in Figure 7.

The SAFS is well delineated by concentrated high-strain (>200 nanostrain/yr). Compared to the prediction of the GNSS-only strain rate model (Figures 7a, 7d and 7g), the integrated InSAR/GNSS model (Figures 7b, 7e and 7h) reveals more focused strain concentration, especially at locations where there is known surface creep (e.g., creeping section of SAFS and Hayward fault). Maacama and Bartlett Springs both have much larger strain concentrations in the InSAR/GNSS model although this may be a consequence of the assumption that the InSAR deformation is parallel to the GNSS deformation. Dilatational strain predicted by the integrated InSAR/GNSS model shows extension in the Central Valley associated with the subsidence from groundwater extraction. The shear component is also larger in areas of known hydrological signals. There is a prominent shear strain anomaly in the InSAR/GNSS strain rate maps (Figures 7e and 7f) that is to the east of and parallel to the creeping section. However, there is not enough GNSS data in the region to determine if this is a real strain-rate anomaly or artifact from the interpolation approach. Overall, the strain is more widely distributed in the integrated InSAR/GNSS model, with significant components being off-fault. Questions remain on how much of this off-fault strain is from tectonic motion versus hydrological activities, and are these signals steady over time or just transients. Answering these questions is key to accurately assessing the strain/moment accumulation and the associated seismic hazards.

4. Conclusion

We developed an approach to integrate the frequent, high-quality, observations from the ascending and descending look directions of the Sentinel-1 INSAR satellites and GNSS time-series (4.5 years) over the entire SAFS. The two components of average LOS velocity were used to refine and update estimates of creep rate along the major strands of the SAFS. The two LOS components were decomposed into 3-components of velocity by assuming the direction of deformation matches those predicted by a GNSS-only velocity model. The higher spatial resolution vector velocity maps were used to estimate the three components of horizontal crustal strain rate.

A video tour of the high-resolution LOS velocity maps reveals a wide array of deformation processes including: active faults and stepovers; extraction and recharge of groundwater, petroleum and geothermal fluids; and continuous expansion of the surface of dry lake beds (Movie S1 and available at https://doi.org/10.18738/T8/334Q29). We see significant off-fault strain, yet challenges remain in separating the contribution from tectonic and hydrologic sources and whether hydrologic strain will increase seismic hazards.

Transient deformation processes (e.g., hydrologic, magmatic, and tectonic) are known having strain rate signals that exceed the 100 nanostrain/yr threshold needed for hazard assessment. However, current strain rate models based only on point GNSS measurements are reliable at longer wavelengths (>30–40 km) and

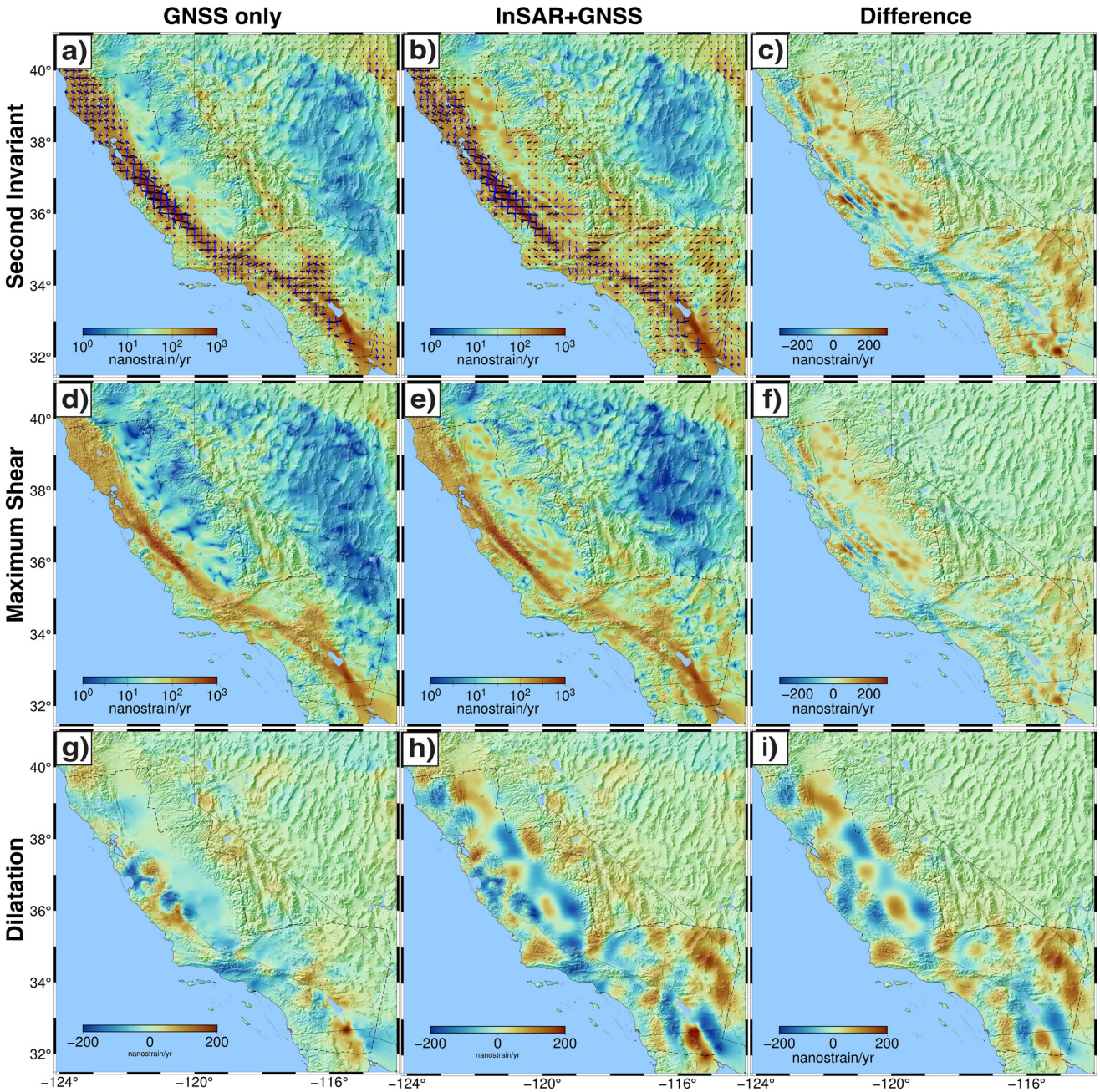

Figure 7. Strain rate maps for San Andreas fault system. Panel (a) is the second invariant of strain rate derived with gpsgridder using Global Navigation Satellite System (GNSS) data only. Black and blue bars represent compressional and extensional principal strain rates respectively, and they are clipped at 100 nanostrain/yr. Panel (b) is same as panel (a), but using decomposed Interferometric Synthetic Aperture Radar + GNSS horizontal velocity components. (c) Differences between Panels (a) and (b). Panels (d and e) Maximum shear strain rate (defined as $\max\left(\dot{\varepsilon}_1 - \dot{\varepsilon}_2\right) / 2$, Savage et al., 2001) maps with panel (f) being their difference. (g and h) Dilatation rate (defined as $\left(\dot{\varepsilon}_1 + \dot{\varepsilon}_2\right)$, Savage et al., 2001) with panel (i) being their difference. In all plots, the dashed bounding box denotes the area with Sentinel-1 coverage from two look directions.

have large differences at shorter wavelengths so they cannot achieve the 100 nanostrain/yr accuracy threshold for assessing seismic hazard. We have demonstrated that integration of the frequent, high-quality, observations from the Sentinel-1 INSAR satellites with frequent, precise GNSS time-series can achieve this level of accuracy at a uniform spatial resolution of 10 km or less over the entire SAFS. Given the 20-year plus observation plan of the twin Sentinel-1 satellites, as well as continued GNSS operations, these high spatial resolution, time-dependent products will continue to improve.

Data Availability Statement

All data are originally available through Sentinel Scientific Data Hub (https://scihub.copernicus.eu) and Alaska Data Search Vertex (https://search.asf.alaska.edu). Data processing are done with the open source InSAR processing software GMTSAR (https://github.com/gmtsar/gmtsar). Processed data are currently available at https://topex.ucsd.edu/gmtsar/insargen, and on the move to SCEC as part of the Community Geodetic Model (https://www.scec.org/research/cgm). The GNSS MEaSUREs displacement time series produced by SIO and the Jet Propulsion Laboratory can be found at the Scripps Orbit and Permanent Array Center (SOPAC) archive (http://garner.ucsd.edu/pub/timeseries/measures/ats/WesternNorthAmerica/). All processed InSAR data are available at Texas Data Repository (https://doi.org/10.18738/T8/NBVNH6).

Acknowledgments
The authors want to thank Jonathan Weiss and another anonymous reviewer for their valuable suggestions. The authors thank the European Space Agency for the extraordinary data open policy on the Sentinel-1 mission and the Alaska Satellite Facility and UNAVCO for archiving the data and the precise orbital products. This study was funded by the NASA Earth Surface and Interior Program (80NSSC19K1043 and NNX17AD99G), the NASA MEaSUREs Program (NNH17ZDA001N), the National Science Foundation, Office of Advanced Cyberinfrastructure (OAC-1834807), and the Southern California Earthquake Center (SCEC) (20074). SCEC is funded by the NSF cooperative Agreement EAR-1033462 and USGS Cooperative Agreement G12AC20038.

References

Bayona, J. A., Savran, W., Strader, A., Hainzl, S., Cotton, F., & Schorlemmer, D. (2021). Two global ensemble seismicity models obtained from the combination of interseismic strain measurements and earthquake-catalogue information. *Geophysical Journal International*, *224*(3), 1945–1955.

Bendat, J. S., & Piersol, A. G. (2011). *Random data: Analysis and measurement procedures (page 204, case 3)*. John Wiley & Sons.

Bock, Y., Moore, A. W., Argus, D. F., Fang, P., Jiang, S., KedarLiu, S. Z., & Sullivan, A. (2021). *Extended Solid Earth Science ESDR System (ES3): Algorithm Theoretical Basis Document, Sept. 19, NASA MEaSUREs project*. Retrieved from http://sopac-csrc.ucsd.edu/wp-content/uploads/2021/08/ESESES-ATBD.pdf

Burford, R. O., & Harsh, P. W. (1980). Slip on the San Andreas fault in central California from alinement array surveys. *Bulletin of the Seismological Society of America*, *70*(4), 1233–1261.

Chen, C. W., & Zebker, H. A. (2002). Phase unwrapping for large SAR interferograms: Statistical segmentation and generalized network models. *IEEE Transactions on Geoscience and Remote Sensing*, *40*(8), 1709–1719. https://doi.org/10.1109/tgrs.2002.802453

Elliott, J. R., Biggs, J., Parsons, B., & Wright, T. J. (2008). InSAR slip rate determination on the Altyn Tagh Fault, northern Tibet, in the presence of topographically correlated atmospheric delays. *Geophysical Research Letters*, *35*(12). https://doi.org/10.1029/2008gl033659

Elliott, J. R., Walters, R. J., & Wright, T. J. (2016). The role of space-based observation in understanding and responding to active tectonics and earthquakes. *Nature Communications*, *7*, 13844. https://doi.org/10.1038/ncomms13844

Emardson, T. R., Simons, M., & Webb, F. H. (2003). Neutral atmospheric delay in interferometric synthetic aperture radar applications: Statistical description and mitigation. *Journal of Geophysical Research: Solid Earth*, *108*(B5). https://doi.org/10.1029/2002jb001781

Field, E. H., Arrowsmith, R. J., Biasi, G. P., Bird, P., Dawson, T. E., Felzer, K. R., et al. (2014). Uniform California earthquake rupture forecast, version 3 (UCERF3)—The time-independent model. *Bulletin of the Seismological Society of America*, *104*(3), 1122–1180. https://doi.org/10.1785/0120130164

Field, E. H., Biasi, G. P., Bird, P., Dawson, T. E., Felzer, K. R., Jackson, D. D., et al. (2015). Long-term time-dependent probabilities for the third Uniform California Earthquake Rupture Forecast (UCERF3). *Bulletin of the Seismological Society of America*, *105*(2A), 511–543. https://doi.org/10.1785/0120140093

Field, E. H., Dawson, T. E., Felzer, K. R., Frankel, A. D., Gupta, V., Jordan, T. H., et al. (2009). Uniform California earthquake rupture forecast, version 2 (UCERF 2). *Bulletin of the Seismological Society of America*, *99*(4), 2053–2107. https://doi.org/10.1785/0120080049

Flesch, L. M., Holt, W. E., Haines, A. J., & Shen-Tu, B. (2000). Dynamics of the Pacific-North American plate boundary in the western United States. *Science*, *287*(5454), 834–836. https://doi.org/10.1126/science.287.5454.834

Hackl, M., Malservaisi, R., & Wdowinski, S. (2009). Strain pattern from dense GPS networks. *Hazards and Earth System Sciences*, *9*, 1177–1187. https://doi.org/10.5194/nhess-9-1177-2009

Haines, A. J., & Holt, W. E. (1993). A procedure for obtaining the complete horizontal motions within zones of distributed deformation from the inversion of strain rate data. *Journal of Geophysical Research*, *98*(B7), 12057–12082. https://doi.org/10.1029/93jb00892

Holt, W. E., & Shcherbenko, G. (2013). Toward a continuous monitoring of the horizontal displacement gradient tensor field in Southern California using cGPS observations from Plate Boundary Observatory (PBO). *Seismological Research Letters*, *84*(3), 455–467. https://doi.org/10.1785/0220130004

Klein, E., Bock, Y., Xu, X., Sandwell, D. T., Golriz, D., Fang, P., & Su, L. (2019). Transient deformation in California from two decades of GPS displacements: Implications for a three-dimensional kinematic reference frame. *Journal of Geophysical Research: Solid Earth*, *124*(11), 12189–12223. https://doi.org/10.1029/2018jb017201

Kreemer, C., Blewitt, G., & Klein, E. C. (2014). A geodetic plate motion and global strain rate model. *Geochemistry, Geophysics, Geosystems*, *15*(10), 3849–3889. https://doi.org/10.1002/2014gc005407

Li, X., Jónsson, S., & Cao, Y. (2021). Interseismic deformation from Sentinel-1 burst-overlap interferometry: Application to the Southern Dead Sea Fault. *Geophysical Research Letters*, *48*(16), e2021GL093481. https://doi.org/10.1029/2021gl093481

Loveless, J. P., & Meade, B. J. (2011). Stress modulation on the San Andreas fault by interseismic fault system interactions. *Geology*, *39*(11), 1035–1038. https://doi.org/10.1130/g32215.1

McCaffrey, R. (2005). Block kinematics of the Pacific–North America plate boundary in the southwestern United States from inversion of GPS, seismological, and geologic data. *Journal of Geophysical Research*, *110*, B07401. https://doi.org/10.1029/2004JB003307

Neely, W. R., Borsa, A. A., & Silverii, F. (2019). GInSAR: A cGPS correction for enhanced InSAR time series. *IEEE Transactions on Geoscience and Remote Sensing*, *58*(1), 136–146.

Pagani, C., Bodin, T., Métois, M., & Lasserre, C. (2021). Bayesian estimation of surface strain rates from GNSS measurements: Application to the Southwestern US. *Journal of Geophysical Research: Solid Earth*, e2021JB021905.

Parsons, T. (2006). Tectonic stressing in California modeled from GPS observations. *Journal of Geophysical Research*, *111*. https://doi.org/10.1029/2005JB003946

Parsons, T., Johnson, K. M., Bird, P., Bormann, J., Dawson, T. E., Field, E. H., et al. (2013). *Appendix C—deformation models for UCERF3.*

Petersen, M. D., Mueller, C. S., Frankel, A. D., & Zeng, Y. (2008). *Spatial seismicity rates and maximum magnitudes for background earthquakes* (No. 2007-1437-J). US Geological Survey.

Petersen, M. D., Zeng, Y., Haller, K. M., McCaffrey, R., Hammond, W. C., Bird, P., et al. (2014). Geodesy- and geology-based slip-rate models for the Western United States (excluding California) national seismic hazard maps. *U.S. Geological Survey Open-File Report*, *2013–1293*, 38. https://doi.org/10.3133/ofr20131293

Platt, J. P., & Becker, T. W. (2010). Where is the real transform boundary in California? *Geochemistry, Geophysics, Geosystems*, *11*, Q06012. https://doi.org/10.1029/2010GC003060

Prats-Iraola, P., Scheiber, R., Marotti, L., Wollstadt, S., & Reigber, A. (2012). TOPS interferometry with TerraSAR-X. *IEEE Transactions on Geoscience and Remote Sensing*, *50*(8), 3179–3188. https://doi.org/10.1109/tgrs.2011.2178247

Rollins, C., Wright, T. J., Weiss, J. R., Hooper, A. J., Walters, R. J., Lazecky, M., et al. (2020). *Tectonic strain rates across the central Alpine-Himalayan Belt from Sentinel-1 InSAR and GNSS observations, and implications for seismic hazard*. In AGU Fall Meeting 2020. AGU.

Sandwell, D. T., & Wessel, P. (2016). Interpolation of 2-D vector data using constraints from elasticity. *Geophysical Research Letters*, *43*(20). https://doi.org/10.1002/2016gl070340

Sandwell, D. T., Zeng, Y., Shen, Z. K., Crowell, B., Murray, J., McCaffrey, R., & Xu, X. (2016). *The SCEC community geodetic model V1: Horizontal velocity grid*. In SCEC Annual Meeting.

Sandwell, D. T., Xu, X., Mellors, R., Wei, M., Tong, X., & Wessel, P. (2016). *GMTSAR: An InSAR processing system based on generic mapping tools* (2nd ed.). Retrieved from http://topex.ucsd.edu/gmtsar/tar/GMTSAR_2ND_TEX.pdf

Savage, J. C., Gan, W., & Svarc, J. L. (2001). Strain accumulation and rotation in the Eastern California Shear Zone. *Journal of Geophysical Research*, *106*(B10), 21995–22007. https://doi.org/10.1029/2000jb000127

Shanker, A. P., & Zebker, H. A. (2009). Sparse two-dimensional phase unwrapping using regular grid methods. *IEEE Geoscience and Remote Sensing Letters*, *6*(3), 519–522. https://doi.org/10.1109/lgrs.2009.2020522

Shen, Z. K., & Liu, Z. (2020). Integration of GPS and InSAR data for resolving 3-dimensional crustal deformation. *Earth and Space Science*, *7*(4), e2019EA001036. https://doi.org/10.1029/2019ea001036

Shen, Z. K., Wang, M., Zeng, Y., & Wang, F. (2015). Optimal interpolation of spatially discretized geodetic data. *Bulletin of the Seismological Society of America*, *105*, 2117–2127. https://doi.org/10.1785/0120140247

Smith-Konter, B. R., Sandwell, D. T., & Shearer, P. (2011). Locking depths estimated from geodesy and seismology along the San Andreas Fault System: Implications for seismic moment release. *Journal of Geophysical Research: Solid Earth*, *116*(B6).

Tape, C., Muse, P., & Simons, M. (2009). Multiscale estimation of GPS velocity fields. *Geophysical Journal International*, *179*, 945–971. https://doi.org/10.1111/j.1365-246x.2009.04337.x

Tong, X., Sandwell, D., & Smith-Konter, B. (2013). High-resolution interseismic velocity data along the San Andreas Fault from GPS and InSAR. *Journal of Geophysical Research: Solid Earth*, *118*, 369–389. https://doi.org/10.1029/2012JB009442

Tong, X., & Schmidt, D. (2016). Active movement of the Cascade landslide complex in Washington from a coherence-based InSAR time series method. *Remote Sensing of Environment*, *186*, 405–415. https://doi.org/10.1016/j.rse.2016.09.008

Tong, X., Smith-Konter, B., & Sandwell, D. T. (2014). Is there a discrepancy between geological and geodetic slip rates along the San Andreas Fault System? *Journal of Geophysical Research: Solid Earth*, *119*, 2518–2538. https://doi.org/10.1002/2013JB010765

Tymofyeyeva, E., & Fialko, Y. (2015). Mitigation of atmospheric phase delays in InSAR data, with application to the Eastern California Shear Zone. *Journal of Geophysical Research: Solid Earth*, *120*(8), 5952–5963. https://doi.org/10.1002/2015jb011886

Tymofyeyeva, E., & Fialko, Y. (2018). Geodetic evidence for a blind fault segment at the southern end of the San Jacinto Fault Zone. *Journal of Geophysical Research: Solid Earth*, *123*, 878–891. https://doi.org/10.1002/2017JB014477

Wang, K., Xu, X., & Fialko, Y. (2017). Improving burst alignment in TOPS interferometry with bivariate enhanced spectral diversity. *IEEE Geoscience and Remote Sensing Letters*, *14*(12), 2423–2427. https://doi.org/10.1109/lgrs.2017.2767575

Ward, L. A., Smith-Konter, B. R., Xu, X., & Sandwell, D. T. (2021). Seismic moment accumulation response to lateral crustal variations of the San Andreas Fault System. *Journal of Geophysical Research: Solid Earth*, *126*(4), e2020JB021208. https://doi.org/10.1029/2020jb021208

Wei, M., Sandwell, D. T., & Smith-Konter, B. (2010). Optimal combination of InSAR and GPS for measuring interseismic crustal deformation. *Advances in Space Research*, *46*, 236–249. https://doi.org/10.1016/j.asr.2010.03.013

Weiss, J. R., Walters, R. J., Morishita, Y., Wright, T. J., Lazecky, M., Wang, H., et al. (2020). High-resolution surface velocities and strain for Anatolia from Sentinel-1 InSAR and GNSS data. *Geophysical Research Letters*, *47*(17), e2020GL087376. https://doi.org/10.1029/2020gl087376

Wessel, P., Luis, J. F., Uieda, L., Scharroo, R., Wobbe, F., Smith, W. H. F., & Tian, D. (2019). The generic mapping tools version 6. *Geochemistry, Geophysics, Geosystems*, *20*(11), 5556–5564. https://doi.org/10.1029/2019gc008515

Wright, T. J., Parsons, B. E., & Lu, Z. (2004). Toward mapping surface deformation in three dimensions using InSAR. *Geophysical Research Letters*, *31*(1). https://doi.org/10.1029/2003gl018827

Xu, X., & Sandwell, D. T. (2019). Toward absolute phase change recovery with InSAR: Correcting for earth tides and phase unwrapping ambiguities. *IEEE Transactions on Geoscience and Remote Sensing*, *58*(1), 726–733.

Xu, X., Sandwell, D. T., Tymofyeyeva, E., González-Ortega, A., & Tong, X. (2017). Tectonic and anthropogenic deformation at the Cerro Prieto geothermal step-over revealed by Sentinel-1A InSAR. *IEEE Transactions on Geoscience and Remote Sensing*, *55*(9), 5284–5292. https://doi.org/10.1109/tgrs.2017.2704593

Xu, X., Ward, L. A., Jiang, J., Smith-Konter, B., Tymofyeyeva, E., Lindsey, E. O., et al. (2018). Surface creep rate of the southern San Andreas fault modulated by stress perturbations from nearby large events. *Geophysical Research Letters*, *45*(19), 10–259. https://doi.org/10.1029/2018gl080137

Zeng, Y., Petersen, M. D., & Shen, Z.-K. (2018). Earthquake potential in California-Nevada implied by correlation of strain rate and seismicity. *Geophysical Research Letters*, *45*, 1778–1785. https://doi.org/10.1002/2017gl075967

Zeng, Y., & Shen, Z.-K. (2016). A fault-based model for crustal deformation, fault slip rates and off-fault strain rate in California. *Bulletin of the Seismological Society of America*, *106*(2), 766–784. https://doi.org/10.1785/0120140250

Zeng, Y., & Shen, Z. K. (2017). A fault-based model for crustal deformation in the Western United States Based on a combined inversion of GPS and geologic inputs. *Bulletin of the Seismological Society of America*, *107*(6), 2597–2612. https://doi.org/10.1785/0120150362

References From the Supporting Information

Bilham, R. (1989). Surface slip subsequent to the 24 November 1987 Superstition Hills, California, earthquake monitored by digital creepmeters. *Bulletin of the Seismological Society of America*, *79*(2), 424–450.

Chaussard, E., Bürgmann, R., Shirzaei, M., Fielding, E. J., & Baker, B. (2014). Predictability of hydraulic head changes and characterization of aquifer-system and fault properties from InSAR-derived ground deformation. *Journal of Geophysical Research: Solid Earth*, *119*(8), 6572–6590. https://doi.org/10.1002/2014jb011266

DeMets, C., Gordon, R. G., Argus, D. F., & Stein, S. (1990). Current plate motions. *Geophysical Journal International*, *101*(2), 425–478. https://doi.org/10.1111/j.1365-246x.1990.tb06579.x

DeMets, C., Gordon, R. G., Argus, D. F., & Stein, S. (1994). Effect of recent revisions to the geomagnetic reversal time scale on estimates of current plate motions. *Geophysical Research Letters*, *21*(20), 2191–2194. https://doi.org/10.1029/94gl02118

Fialko, Y., & Simons, M. (2000). Deformation and seismicity in the Coso geothermal area, Inyo County, California: Observations and modeling using satellite radar interferometry. *Journal of Geophysical Research*, *105*(B9), 21781–21793. https://doi.org/10.1029/2000jb900169

Fielding, E. J., Blom, R. G., & Goldstein, R. M. (1998). Rapid subsidence over oil fields measured by SAR interferometry. *Geophysical Research Letters*, *25*(17), 3215–3218. https://doi.org/10.1029/98gl52260

Jiang, J., & Lohman, R. B. (2021). Coherence-guided InSAR deformation analysis in the presence of ongoing land surface changes in the Imperial Valley, California. *Remote Sensing of Environment*, *253*, 112160. https://doi.org/10.1016/j.rse.2020.112160

Lanari, R., Lundgren, P., Manzo, M., & Casu, F. (2004). Satellite radar interferometry time series analysis of surface deformation for Los Angeles, California. *Geophysical Research Letters*, *31*(23). https://doi.org/10.1029/2004gl021294

Lienkaemper, J. J., Borchardt, G., & Lisowski, M. (1991). Historic creep rate and potential for seismic slip along the Hayward fault, California. *Journal of Geophysical Research*, *96*(B11), 18261–18283. https://doi.org/10.1029/91jb01589

Ojha, C., Shirzaei, M., Werth, S., Argus, D. F., & Farr, T. G. (2018). Sustained groundwater loss in California's Central Valley exacerbated by intense drought periods. *Water Resources Research*, *54*(7), 4449–4460. https://doi.org/10.1029/2017wr022250

Ruch, J., Warren, J. K., Risacher, F., Walter, T. R., & Lanari, R. (2012). Salt lake deformation detected from space. *Earth and Planetary Science Letters*, *331*, 120–127. https://doi.org/10.1016/j.epsl.2012.03.009

Smith-Konter, B., & Sandwell, D. (2009). Stress evolution of the San Andreas fault system: Recurrence interval versus locking depth. *Geophysical Research Letters*, *36*(13).

Sneed, M., & Brandt, J. T. (2020). Mitigating land subsidence in the Coachella Valley, California, USA: An emerging success story. *Proceedings of the International Association of Hydrological Sciences*, *382*, 809–813. https://doi.org/10.5194/piahs-382-809-2020

Tymofyeyeva, E., Fialko, Y., Jiang, J., Xu, X., Sandwell, D., Bilham, R., et al. (2019). Slow slip event on the southern San Andreas fault triggered by the 2017 M w 8.2 Chiapas (Mexico) earthquake. *Journal of Geophysical Research: Solid Earth*, *124*(9), 9956–9975. https://doi.org/10.1029/2018jb016765

Wei, M., Sandwell, D., & Fialko, Y. (2009). A silent Mw 4.7 slip event of October 2006 on the Superstition Hills fault, southern California. *Journal of Geophysical Research*, *114*(B7). https://doi.org/10.1029/2008jb006135

Wisely, B. A., & Schmidt, D. (2010). Deciphering vertical deformation and poroelastic parameters in a tectonically active fault-bound aquifer using InSAR and well level data, San Bernardino basin, California. *Geophysical Journal International*, *181*(3), 1185–1200. https://doi.org/10.1111/j.1365-246x.2010.04568.x

Xu, X., Sandwell, D. T., & Smith-Konter, B. (2020a). Coseismic displacements and surface fractures from Sentinel-1 InSAR: 2019 Ridgecrest earthquakes. *Seismological Research Letters*, *91*(4), 1979–1985. https://doi.org/10.1785/0220190275

Xu, X., Sandwell, D. T., Ward, L. A., Milliner, C. W., Smith-Konter, B. R., Fang, P., & Bock, Y. (2020b). Surface deformation associated with fractures near the 2019 Ridgecrest earthquake sequence. *Science*, *370*(6516), 605–608. https://doi.org/10.1126/science.abd1690